Ultra-stable and versatile widefield cryo-fluorescence microscope for single-molecule localization with sub-nanometer accuracy

Weixing Li,[1,2] **Simon C. Stein,**[2] **Ingo Gregor,**[2] **and Jörg Enderlein,**[1,2,*]

[1] *DFG Research Center 'Nanoscale Microscopy and Molecular Physiology of the Brain' (CNMPB), Göttingen, Germany*
[2] *Third Institute of Physics, Georg-August University, 37077 Göttingen, Germany*
[*] *jenderl@gwdg.de*

www.joerg-enderlein.de

Abstract: We developed a stand-alone cryostat with optical access to the sample which can be adapted to any epi-fluorescence microscope for single-molecule fluorescence spectroscopy and imaging. The cryostat cools the sample to a cryogenic temperature of 89 K, and allows for imaging single molecules using an air objective with a numerical aperture of 0.7. An important property of this system is its excellent thermal and mechanical stability, enabling long-time observations of samples over several hours with negligible drift. Using this system, we performed photo-bleaching studies of Atto647N dye molecules, and find an improvement of the photostability of these molecules by more than two orders of magnitude. The resulting increased photon numbers of several millions allow for single-molecule localization accuracy of sub-nanometer.

OCIS codes: (180.2520) Fluorescence microscopy; (100.6640) Superresolution.

References and links

1. A. Briegel, S. Chen, A. J. Koster, M. Plitzko, C. L. Schwartz, and G. J. Jensen, "Correlated Light and Electron Cryo-Microscopy," Methods Enzymol. **481**, 317–341 (2010).
2. Y.-W. Chang, S. Chen, E. I. Tocheva, A. Treuner-Lange, S. Löbach, L. Søgaard-Andersen, and G. J. Jensen, "Correlated cryogenic photoactivated localization microscopy and cryo-electron tomography," Nat. Methods **11**, 737–739 (2014).
3. S. Weisenburger, B. Jing, D. Hänni, L. Reymond, B. Schuler, A. Renn, and V. Sandoghdar, "Cryogenic colocalization microscopy for nanometer-distance measurements," Phys. Chem. Chem. Phys. **15**, 763–770 (2014).
4. R. Kaufmann, P. Schellenberger, E. Seiradake, I. M. Dobbie, E. Y. Jones, I. Davis, C. Hagen, and K. Grünewald, "Super-resolution microscopy using standard fluorescent proteins in intact cells under cryo-conditions," Nano Lett. **14**, 4171–4175 (2014).
5. V. Hirschfeld, H. Paulsen, and C. G. Hübner, "The spectroscopic ruler revisited at 77 K," Phys. Chem. Chem. Phys. **15**, 17664–17671 (2013).
6. M. Hussels, A. Konrad, and M. Brecht, "Confocal sample-scanning microscope for single-molecule spectroscopy and microscopy with fast sample exchange at cryogenic temperatures," Rev. Sci. Instrum. **83**, 123706 (2012).
7. C. L. Schwartz, V. I. Sarbash, F. I. Ataullakhanov, J. R. McIntosh, and D. Nicastro, "Cryo-fluorescence microscopy facilitates correlations between light and cryo-electron microscopy and reduces the rate of photobleaching," J. Microsc. **227**, 98–109 (2007).

#223365 - $15.00 USD Received 19 Sep 2014; revised 20 Nov 2014; accepted 21 Nov 2014; published 6 Feb 2015

8. A. Sartori, R. Gatz, F. Beck, A. Rigort, W. Baumeister, and J. M. Plitzko, "Correlative microscopy: Bridging the gap between fluorescence light microscopy and cryo-electron tomography," J. Struct. Biol. **160**, 135–145 (2007).
9. M. J. Rust, M. Bates, and X. Zhuang, "Sub-diffraction-limit imaging by stochastic optical reconstruction microscopy (storm)," Nat. Methods **3**, 793–796 (2006).
10. E. Betzig, G. H. Patterson, R. Sougrat, O. W. Lindwasser, S. Olenych, J. S. Bonifacino, M. W. Davidson, J. Lippincott-Schwartz, and H. F. Hess, "Imaging intracellular fluorescent proteins at nanometer resolution," Science **313**, 1642–1645 (2006).
11. S. T. Hess, T. P. K Girirajan, and M. D. Mason, "Ultra-high resolution imaging by fluorescence photoactivation localization microscopy," Biophys. J. **91**, 4258–4272 (2006).
12. R. Zondervan, F. Kulzer, M. A. Kol'chenk, and M. Orrit, "Photobleaching of Rhodamine 6G in poly(vinyl alcohol) at the ensemble and single-molecule levels," J. Phys. Chem. A **108**, 1657–1665 (2004).
13. B. Kozankiewicz and M. Orrit, "Single-molecule photophysics, from cryogenic to ambient conditions," Chem. Soc. Rev. **43**, 1029–1043 (2014).
14. J. R. Bellare, H. T. Davis, L. E. Scriven, and Y. Talmon, "Controlled environment vitrification system: an improved sample preparation technique," J. Electron Micr. Tech. **10**, 87–111 (1988).
15. K. L. McDonald, "A review of high-pressure freezing preparation techniques for correlative light and electron microscopy of the same cells and tissues," J. Microsc. **235**, 273–281 (2009).
16. J. Dubochet, "Cryo-EM-the first thirty years," J. Microsc. **245**, 221–224 (2012).
17. L. F. van Driel, J. A. Valentijn, K. M. Valentijn, R. I. Koning, and A. J. Koster, "Tools for correlative cryo-fluorescence microscopy and cryo-electron tomography applied to whole mitochondria in human endothelial cells," Eur. J. Cell Biol. **88**, 669–684 (2009).
18. A. Rigort, F. J. B. Bäuerlein, A. Leis, M. Gruska, C. Hoffmann, T. Laugks, U. Böhm, M. Eibauer, H. Gnaegi, W. Baumeister, and J. M. Plitzko, "Micromachining tools and correlative approaches for cellular cryo-electron tomography," J. Struct. Biol. **172**, 169–179 (2010).
19. M. A. Le Gros, G. McDermott, M. Uchida, C. G. Knoechel, and C. A. Larabell, "High-aperture cryogenic light microscopy," J. Microsc. **235**, 1–8 (2009).
20. W. Kukulski, M. Schorb, S. Welsch, A. Picco, M. Kaksonen, and J. A. G. Briggs, "Correlated fluorescence and 3D electron microscopy with high sensitivity and spatial precision," J. Cell Biol. **192**, 111–119 (2011).
21. R. Kaufmann, C. Hagen, and K. Grünewald, "Fluorescence cryo-microscopy: current challenges and prospects," Curr. Opin. Cell Biol. **20**, 86–91 (2014).
22. V. Hirschfeld and C. G. Hübner, "A sensitive and versatile laser scanning confocal optical microscope for single-molecule fluorescence at 77 K," Rev. Sci. Instrum. **81**, 113705 (2010).
23. R. Henriques, M. Lelek, E. F. Fornasiero, F. Valtorta, C. Zimmer, and M. M. Mhlanga, "Quickpalm: 3d real-time photoactivation nanoscopy image processing in ImageJ," Nat. Methods **7**, 339–340 (2010).
24. C. A. Schneider, W. S. Rasband, and K. W. Eliceiri, "NIH image to ImageJ: 25 years of image analysis," Nat. Methods **9**, 671–675 (2012).
25. J. Enderlein, E. Toprak, and P. R. Selvin, "Polarization effect on position accuracy of fluorophore localization," Opt. Express **14**, 8111–8120 (2006).
26. S. Wolter, A. Loschberger, T. Holm, S. Aufmkolk, M. C. Dabauvalle, S. van de Linde, and M. Sauer, "RapidStorm: accurate, fast open-source software for localization microscopy," Nat. Methods **9**, 1040–1041 (2012).
27. K. I. Mortensen, L. S. Churchman, J. A. Spudich, and H. Flyvbjerg, "Optimized localization analysis for single-molecule tracking and super-resolution microscopy," Nat. Methods **7**, 377–381 (2010).

---

1. Introduction

In recent years, cryo-fluorescence microscopy (cryo-FM) has been increasingly applied in the field of correlative electron and optical microscopy [1, 2], single molecule fluorescence localization microscopy [3, 4], and single molecule spectroscopy [5, 6]. Correlative measurements bridging cryo-FM and cryo X-ray or electron microscopy combine the specificity of fluorescent labeling with molecular resolution, thus assisting the identification of structural details in biological samples [2, 7, 8]. In combination with super-resolution fluorescence microscopy techniques such as Stochastic Optical Reconstruction Microscopy (STORM) [9] or (Fluorescence) Photoactivation Localization Microscopy ((F)PALM) [10, 11], cryo-FM benefits from an increased photon yield due to the enhanced photostability of the fluorophores at cryogenic temperatures [7, 12, 13]. This results in an exceptional high single-molecule localization accuracy and improved optical resolution [3].

A crucial component for a cryo-FM system is a dedicated cryostat which has to satisfy several experimental requirements. For correlative measurements, samples are typically vitrified with a rapid freezing technique such as plunge freezing [14] or high pressure freezing [15]. These techniques preserve cellular structures in a near-native state by converting liquid water into amorphous ice. Therefore, the cryostat must have the ability to load and transfer vitrified samples below the glass transition temperature of water ($\sim$135 K) to prevent ice crystal formation [16]. In currently existing cryostats for correlative measurements [7, 8, 17–20], the sample is typically embedded in a circling cold dry nitrogen atmosphere to prevent ice condensation, and is cooled by the circulation of a cryogen via an attached piping system, which introduces considerable mechanical instability to the system. In addition, the microscope objective is typically exposed to the cooled optical window or even directly to the frozen sample, thus inducing considerable thermal stress on the objective which results in large optical aberrations [21]. Moreover, ice condensation may occur on the sample and the inner surface of the optical window due to the imperfect dehydration of the nitrogen atmosphere, or on the outer surface of the optical window due to a humid environment, which also lowers the optical performance of such systems.

Vacuum insulated cryostats [6, 22] provide higher thermal and mechanical stability, and are thus usually employed for single-molecule fluorescence microscopy [3] and spectroscopy [5,6]. These cryostats are typically cooled by a continuous circulation of a cryogen [3] or by a static cryogen reservoir [6, 22] using liquid helium (LHe) or liquid nitrogen (LN2). In these designs, the sample is directly attached to the cooling source. As a consequence, any vibration or coolant bubbling is directly transmitted to the sample, causing considerable mechanical instability [21]. Although the use of LHe assures a more stable coolant flow and less bubbling than LN2, the helium consumption and the complex recycling system significantly increase the operational cost. Another major limitation of these vacuum-based cryostats is that the sample can only be gradually cooled inside the cryostat. This makes the observation of vitrified samples and correlative measurements rather difficult, due to the impossibility to transfer and change samples at cryogenic temperatures.

To overcome all these limitations, we designed and built a cryostat which combines high thermal and mechanical stability for single-molecule imaging with the ability of transferring and changing samples at cryogenic temperatures for correlative measurements. Our cryostat is a vacuum-insulated, stand-alone device using static liquid nitrogen cooling without any circulation accessories. The design mechanically decouples the sample from any unstable parts of the cryostat, thus providing an exceptional high mechanical stability. This enables long-time observations of samples for several hours with negligible mechanical drift. The cryostat can be integrated into any conventional inverted epi-fluorescence microscope, and allows for the use of any air objective with a working distance of 1.5 mm. The optical design delivers superior single-molecule imaging quality with negligible spherical aberration and field distortion. Using our system, we investigated the photostability enhancement of Atto647N molecules and and find enhancement factors of more than two orders of magnitude at 89 K. This allows us to localize single molecules with sub-nanometer accuracy after applying a simple, software-based correction of the residual drift.

2. Experimental setup

The goal of the design of the cryostat is to provide high thermal and mechanical stability, and to be compatible with conventional inverted epi-fluorescence microscopes which use high-quality air objectives. Furthermore, easy sample change at cryogenic temperatures was also an important design goal. The cryostat (Fig. 1) consists of two vessels: The inner vessel serves as a tank which contains $\sim$1.5 L LN2 as the coolant. This inner LN2 tank is sealed into an outer vessel (vacuum housing), and between the tank and the outer housing vessel, a vacuum is generated for thermal insulation. On the bottom of the vacuum housing, an intermediate

#223365 - $15.00 USD Received 19 Sep 2014; revised 20 Nov 2014; accepted 21 Nov 2014; published 6 Feb 2015

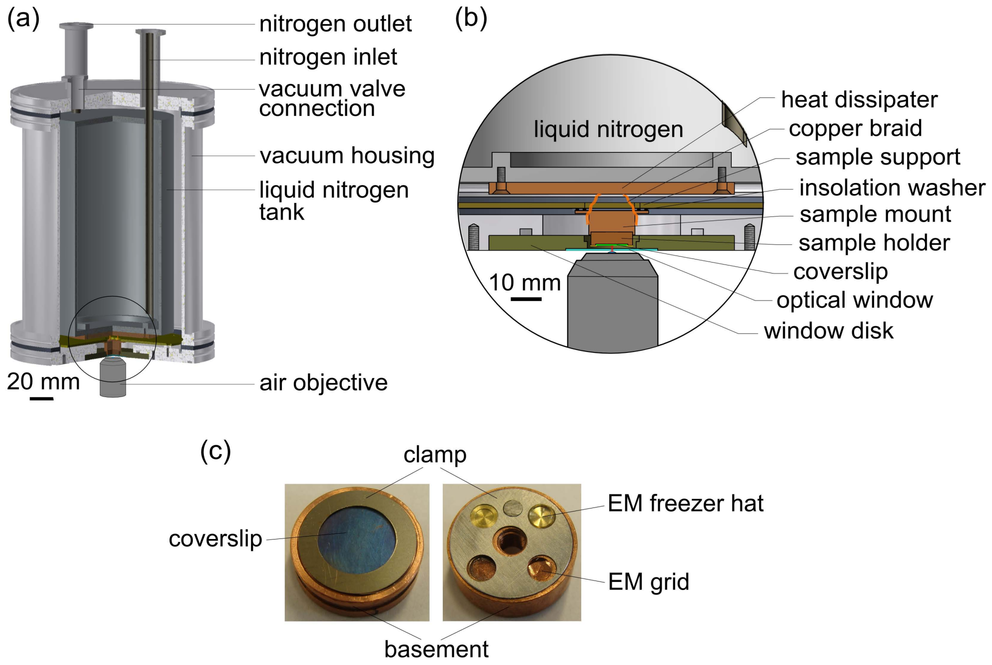

Fig. 1. Design of the cryostat (essential parts shown). (a) Cutaway view of the cryostat accommodating an air objective. (b) Zoom-in view of the central part (black circle in A), showing a sample on a coverslip being imaged by an air objective. (c) Photos of two types of sample holders for standard coverslip and EM grids/freezer hats.

plate (sample support) is fixed to hold the sample mount. Between this sample support plate (made of stainless steel) and the sample mount (made of oxygen free copper), special thermal insulation washers made of polyimide are sandwiched to minimize heat loss. The LN2 tank and the sample mount are shielded by reflective metal sheets (not shown in the figure) to block external thermal radiation. All contact surfaces which may transfer heat are coated with Indium to maximize heat conduction.

The sample mount is connected to a heat dissipater (a copper disc with high thermal conductivity which is fixed on the bottom of the LN2 tank) via flexible copper braids. These braids do not only transfer the heat from the sample mount to the LN2 tank, but also mechanically decouple the sample mount from any other unstable parts of the cryostat, and thus resulting in a high mechanical stability of the sample.

Two types of sample holders (made of oxygen free copper) have been designed to adapt either one coverslip or four EM grids/freezer hats (Fig. 1(c)). The sample holder is loaded into the cryostat through a circular aperture on the bottom of the vacuum housing, and is kept in place on the sample mount by small magnets integrated inside both parts. This aperture is then closed by a metal disc (window disc), which contains a 0.5 mm thick quartz window. This window gives direct optical access to the sample for any air objective with a working distance of 1.5 mm.

After sample loading and closing the window disc, a vacuum of $\sim 1 \times 10^{-2}$ Pa is generated inside the cryostat using a turbo pump (HiCube, Pfeiffer Vacuum GmbH, Germany). This high quality vacuum does not only provide optimal thermal insulation for the cooled sample, but

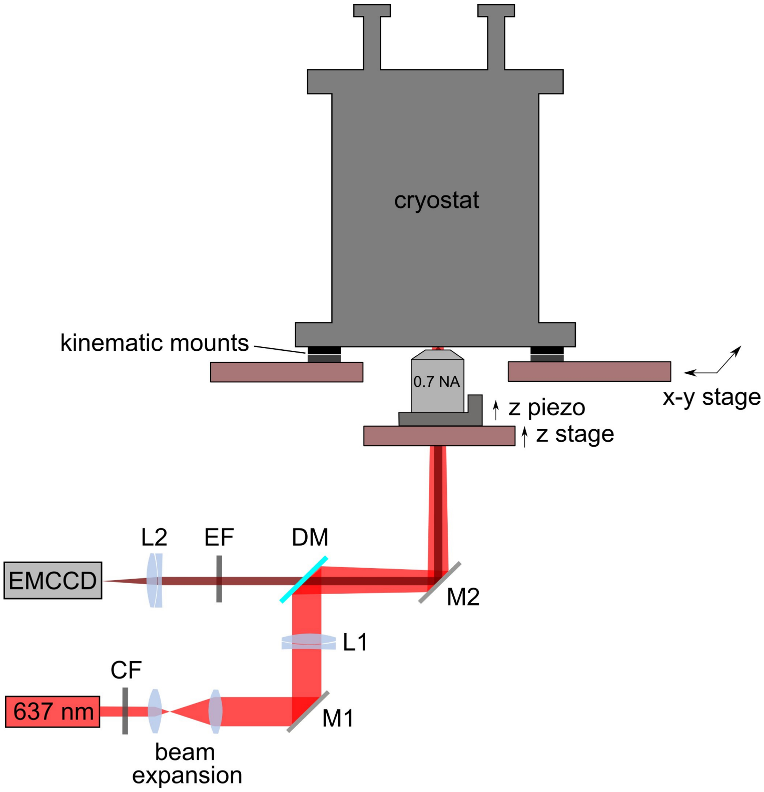

Fig. 2. Schematic depiction of the cryo-fluorescence microscope. Light from a 637 nm laser (OEM-SD-637-500, Changchun New Industries Optoelectronics Tech. Co., Ltd., China) is sent through a clean-up filter CF (HC 640/14, Semrock, NY, USA), expanded by a telescope, and focused by an achromatic lens L1 onto the back focal plane of an air objective (LUCPLFLN, Olympus, 60×, 0.7 NA), after being reflected by a dichroic mirror DM (ET FITC/Cy3/Cy5, Chroma, Bellows Falls, VT, USA) and a mirror M2. The emitted light from the sample is collected by the same objective, sent through an emission filter EF (ET 685/50, Chroma), and focused onto an EMCCD camera (iXon Ultra 897, Andor Technology) by an achromatic doublet lens L2 (AC508-300-A-ML, $f = 300$ mm, Thorlabs GmbH, Germany). The objective is mounted on a z-piezo actuator (PIFOC, Physik Instrumente GmbH, Germany), which itself is fastened on a motorized z-stage, thus allowing for fine and course focusing, respectively. The cryostat is placed on an x-y stage for horizontal motion with respect to the objective via kinematic mounts (KBS98, Thorlabs GmbH, Germany).

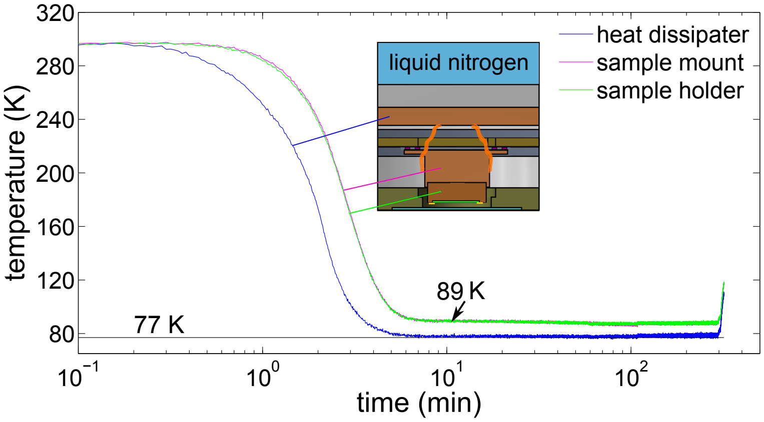

Fig. 3. Cooling efficiency and thermal stability. Temperatures of the heat dissipater, the sample mount, and the sample holder (inset) were measured simultaneously at a sampling frequency of 2 Hz for more than six hours using embedded thermal sensors.

also prevents ice sublimation and water condensation on the sample or on the window surfaces. Moreover, this vacuum-based thermal decoupling prevents any thermal stress on the air objective, which is kept at ambient temperature, thus assuring high optical performance and imaging quality.

The cryostat is integrated into a custom-built inverted epi-fluorescence microscope (Fig. 2). To move the sample with respect to the imaging objective, the cryostat is placed on a motorized x-y stage. The mounting which is done via kinematic mounts allows for easy and reversible placement of the cryostat on the microscope for convenient sample change. The high precision of the kinematic mounts and the large weight of the cryostat ($\sim$14 kg without LN2) assure sufficient mechanical stability without the need for additional fixation.

The epi-fluorescence microscope itself uses a 637 nm continuous wave (cw) laser of 500 mW power for sample illumination. For the used air objective, the field of view of $\sim$80 µm × 80 µm is illuminated with a maximum irradiance of $\sim$3 kW cm^{-2}. The emitted fluorescent light from the sample is collected by the same objective and imaged onto an EMCCD camera. The original Olympus tube lens (f =180 mm) has been replaced by an achromatic doublet lens (f =300 mm), which increases the imaging magnification to 100×. This magnification matches the pixel size of the EMCCD to approximately one fifth of the size of the point spread function (PSF) as is needed for precise single molecule localization, see below.

3. Experimental results

3.1. Cooling efficiency

As a first step, we examined the cooling efficiency and thermal stability of the system. Prior to cooling, the air in the cryostat was evacuated using a turbo pump to produce a vacuum of $\sim 1\times10^{-2}$ Pa. Then, liquid nitrogen was fed into the tank using a transfer line. The rapidly cooled LN2 tank acted as a ”molecule catcher”, which further reduced the vacuum to ca. 1×10^{-3} Pa. After filling the tank, the vacuum pipe and the LN2 transfer line were detached from the cryostat, leaving it as a stand-alone device decoupled from all external mechanical perturbations. During microscope operation, the outlet channel of the LN2 tank was left open to release the gently evaporating nitrogen gas. The temperature on the essential parts – the heat dissipater, the sample mount, and the sample holder – was monitored using embedded thermal

#223365 - $15.00 USD Received 19 Sep 2014; revised 20 Nov 2014; accepted 21 Nov 2014; published 6 Feb 2015

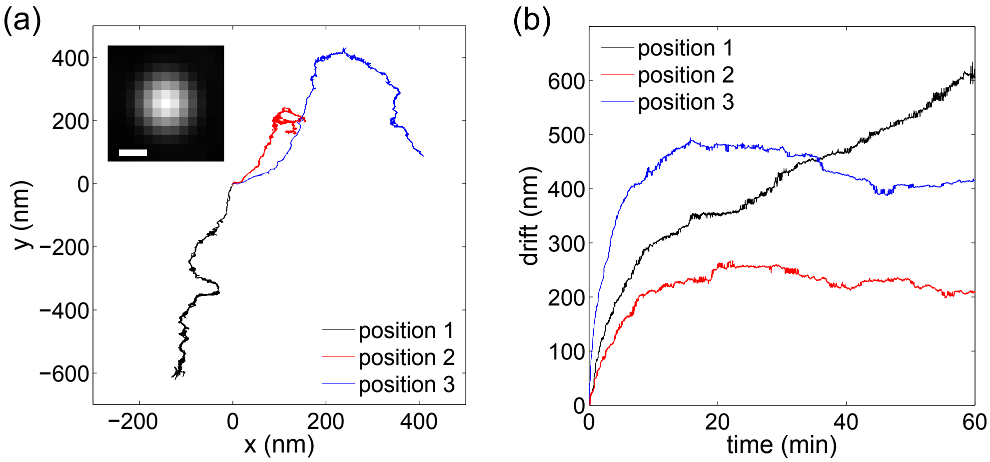

Fig. 4. Lateral sample drift at 89 K. (a) Trajectory of the center position of a fluorescent bead (inset, scale bar 500 nm) measured for one hour. (b) Lateral sample drift quantified as the absolute distance of the bead center position with respect to the starting point.

sensors (PT100 S234PD12, Telemeter Electronic GmbH, Germany).

As shown in Fig. 3, the temperature of the heat dissipater dropped from 294 K to the boiling point of liquid nitrogen (77 K) within six minutes. The temperature of the sample mount and sample holder closely followed this drop and reached thermal equilibrium at 89 K after about eight minutes. Then, all temperature values remained steady for more than six hours with negligible thermal fluctuation (<0.1 K).

This fast cooling rate of more than 0.5 K s^{-1} demonstrates an excellent cooling efficiency through the copper braids, thus enabling an almost instant start of cryo-experiments after tank filling. The identical temperature of sample mount and sample holder indicates a seamless heat transfer through the physical contact between these two parts. The high thermal stability over several hours allows for continuous long-lasting experiments. This working time can be limitless extended by refilling the LN2 tank. The liquid nitrogen evaporation rate of ∼1.5 L over six hours is economic in comparison to other cooling schemes based on the circulation of cryogens, especially liquid helium.

3.2. Mechanical stability

To investigate the mechanical stability of the sample at cryo temperature, we imaged fluorescent beads of 500 nm diameter (Life Technologies GmbH, Germany) at 89 K for one hour with a rate of 2 Hz (exposure time 0.4 s). The bead images (Fig. 4(a) inset) were fitted with a two-dimensional Gaussian distribution using the quickPALM [23] routine in ImageJ [24], which yielded their center positions. The brightness of these beads provided a localization accuracy of a few nanometers. By plotting their center positions as a function of measurement time, we tracked the mechanical drift of the sample with respect to the objective (Fig. 4). This measurement was repeated at three different positions by moving the cryostat several millimeters with respect to the objective to image a different location on the sample.

The data in Fig. 4 show that the sample underwent a moderate drift of less than one micrometer within one hour. Remarkably, for most of the experiments we performed later, the sample drift exhibited a profile similar to the measurements at positions 2 and 3: A fast relaxation within the first ∼ten minutes is followed by minimal fluctuations of several tens of nanometers

#223365 - $15.00 USD Received 19 Sep 2014; revised 20 Nov 2014; accepted 21 Nov 2014; published 6 Feb 2015

over several hours. We also observed that for positions closer to the center of the sample, the total drift value is reduced. We attribute this drift behavior to the thermo-mechanical relaxation of the sample holder which is locally heated by the excitation laser. However, the embedded thermal sensors did not register any temperature change after switch-on of the laser illumination. Although we cannot rule out laser-induced local sample heating (because we do not measure the temperature directly on the sample surface), this effect should be rather minimal due to the efficient heat dissipation. Moreover, we did not observe any defocussing of the image over one hour, which indicates a negligible drift along the vertical direction. This is further confirmed by our long-time single molecule imaging measurements over more than four hours, see section IV.

These excellently low drift values along all three dimensions demonstrate a successful mechanical decoupling of the sample, through flexible metal connections, from other unstable components of the cryostat. The lateral drift of less than one micrometer per hour and the negligible vertical drift exhibit, to our knowledge, the highest mechanical stability of all currently existing devices. This allows for long-time observations of the sample over several hours without any need of complicated active drift-correction methods.

3.3. Changing samples at cryogenic temperatures

Sample change at cryogenic temperatures must avoid any exposure to humid air to prevent ice condensation, and it should be carried out below the glass transition temperature of water (about 135 K) to avoid ice crystal formation in the sample. To meet these two requirements, we developed a workstation (Fig. 5(a)) and a protocol for intact sample change at cryogenic temperatures.

The workstation is based on an acrylic glass box that insulates the sample from the humid environment. Prior to sample change, the Plexiglas box is pre-flushed with nitrogen gas to create a relative dry environment (rel. humidity ∼20%) isolated from the lab air (humidity ∼65% in March). To establish a "perfectly dry" and cold environment for sample change, the liquid nitrogen from the storage dewar is streamed through a long copper pipe for heating to generate a cold gas stream. This cold and dry nitrogen gas is gently supplied to the vacuum chamber of the cold cryostat – either pre-cooled for sample loading, or containing a cold sample for transfer. When the pressure inside the cryostat reaches atmospheric pressure, the window disc can be opened (Fig. 5(b)). Then, a stronger nitrogen flow is applied, and a "cold dry nitrogen curtain" is flushed down around the sample. Under this gas curtain, the sample can be safely transferred to/from a small LN2 storage dewar below the glass transition temperature of 135 K without any ice condensation (Fig. 5(c)). After sample change, the nitrogen curtain is stopped by terminating the nitrogen supply. Then the window disc is quickly closed (Fig. 5(d)), and the vacuum is regenerated. We confirmed the success of this cryo-transfer protocol by loading a sample to a pre-cooled cryostat under the cold nitrogen curtain, and were able to image single molecules without any contamination of ice crystal formed from water vapor. During the whole transfer-procedure, the temperature on the sample mount has been kept steadily at ∼115 K (measured with embed thermal sensor).

The ability to transfer the sample below the glass transition temperature of water enables the correlative measurements of fluorescence microscopy with electron or X-ray microscopy. Also, this allows us to image multiple samples in series without having to warm up the cryostat, which dramatically increases the working efficiency.

3.4. Imaging quality

To achieve highest imaging quality, we employed a high-quality air objective (LUCPLFLN, Olympus) with coverslip thickness correction for up to 1.3 mm to compensate for aberrations

#223365 - $15.00 USD Received 19 Sep 2014; revised 20 Nov 2014; accepted 21 Nov 2014; published 6 Feb 2015

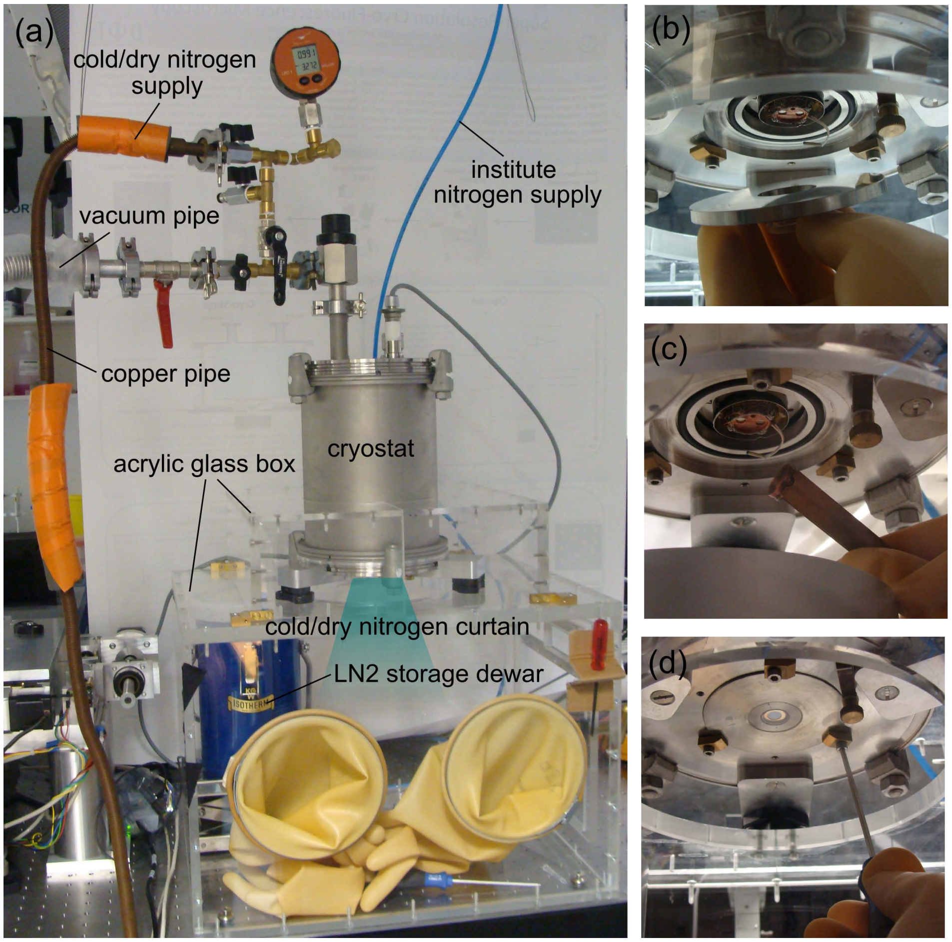

Fig. 5. Workstation for sample change at cryogenic temperatures.

created by the 0.5 mm thick optical window. Moreover, to minimize any background created by the back-reflection of the excitation laser or by (auto-)fluorescent impurities, we used fused silica instead of glass coverslips, and coated the sample holder with a non-reflective and non-fluorescent layer.

To examine the imaging quality, we spin-coated the diluted solution of Atto647N (ATTO-TEC GmbH, Germany) on a fused silica coverslip, and recorded images of single molecules at 89 K with an exposure time of one second and EM gain of 100 (Fig. 6). When the sample is in focus (Figs. 6(a)–6(c)), single molecules can be identified with excellent signal-to-noise ratio. Even the first-order ring of the diffraction pattern is recognizable (Figs. 6(b) and 6(c)). More remarkably, after defocusing by moving the objective 3 μm towards the sample, single molecule image can still be clearly resolved (Figs. 6(d)–6(f)). These defocused patterns appear to be identical in shape across the whole field of view (Fig. 6(d)) with rotationally symmetric intensity profiles (Figs. 6(e) and 6(f)), which indicates a superior imaging quality with minimal field distortion and spherical aberration.

These data show that despite its relatively low numerical aperture, the air objective of 0.7 NA (which has 30% collection efficiency compared to an 1.4 NA oil immersion objective) can

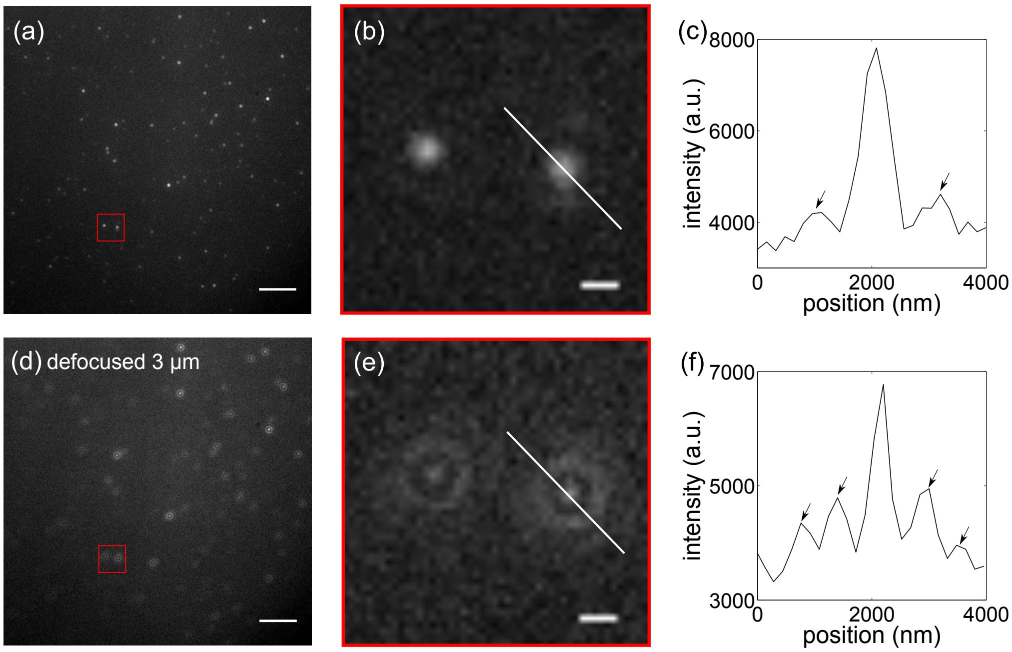

Fig. 6. Single molecule images of Atto647N at 89 K. (A, D) The whole field of view of 80 µm × 80 µm as captured by the EMCCD. Scale bar 10 µm. (B, E) Zoom-in view on the red square in A and D. Scale bar 1 µm. (C, F) Intensity profile along the line in B and E. Arrows point to the side rings of the diffraction pattern.

still record single molecule images with high signal-to-noise ratio. In fact, the air objective is advantageous in comparison to a high NA immersion objective when localizing molecules with fixed emission dipole axis: Imaging with a low NA objective is insensitive to the orientation of the emitter's dipole [25], which drastically simplifies the localization analysis based on PSF fitting. Moreover, imaging with the air objective is also less sensitive to the vertical drift due to its larger focal depth, which is especially beneficial for long-term observations of a sample.

4. Application: Single molecule localization with sub-nanometer accuracy

4.1. Photostability of Atto647N at 294 K *and* 89 K

To study the photostability enhancement of an organic dye upon cooling to cryogenic temperature, we have chosen Atto674N molecules as an example, and examined their photobleaching behavior at 294 K and 89 K on the single molecule level. We spin-coated a diluted aqueous solution of Atto647N on a fused silica coverslip (cleaned by flaming it with a Bunsen burner to remove any fluorescent impurities, and plasma treated to hydrophilize the surface), excited the sample with a 637 nm cw-laser with an irradiance of ~300 W cm^{-2}, and recorded a consecutive series of images at 294 K (see Media 1) and at 89 K (see Media 2) with a frame rate of 0.5 Hz and 1 Hz, respectively.

To evaluate the photobleaching behavior, we counted the number of molecules in each frame to investigate how it changed over time (Fig. 7). At 294 K, almost all molecules were photobleached after about three minutes (Fig. 7(a)), whereas at 89 K, still 31% of the molecules were fluorescent after ~four hours (Fig. 7(b)). As shown in Fig. 7(c), the ratio between the half-life period at 294 K (~20 s) and at 89 K (~7600 s) suggests an photostability enhancement by a

#223365 - $15.00 USD Received 19 Sep 2014; revised 20 Nov 2014; accepted 21 Nov 2014; published 6 Feb 2015

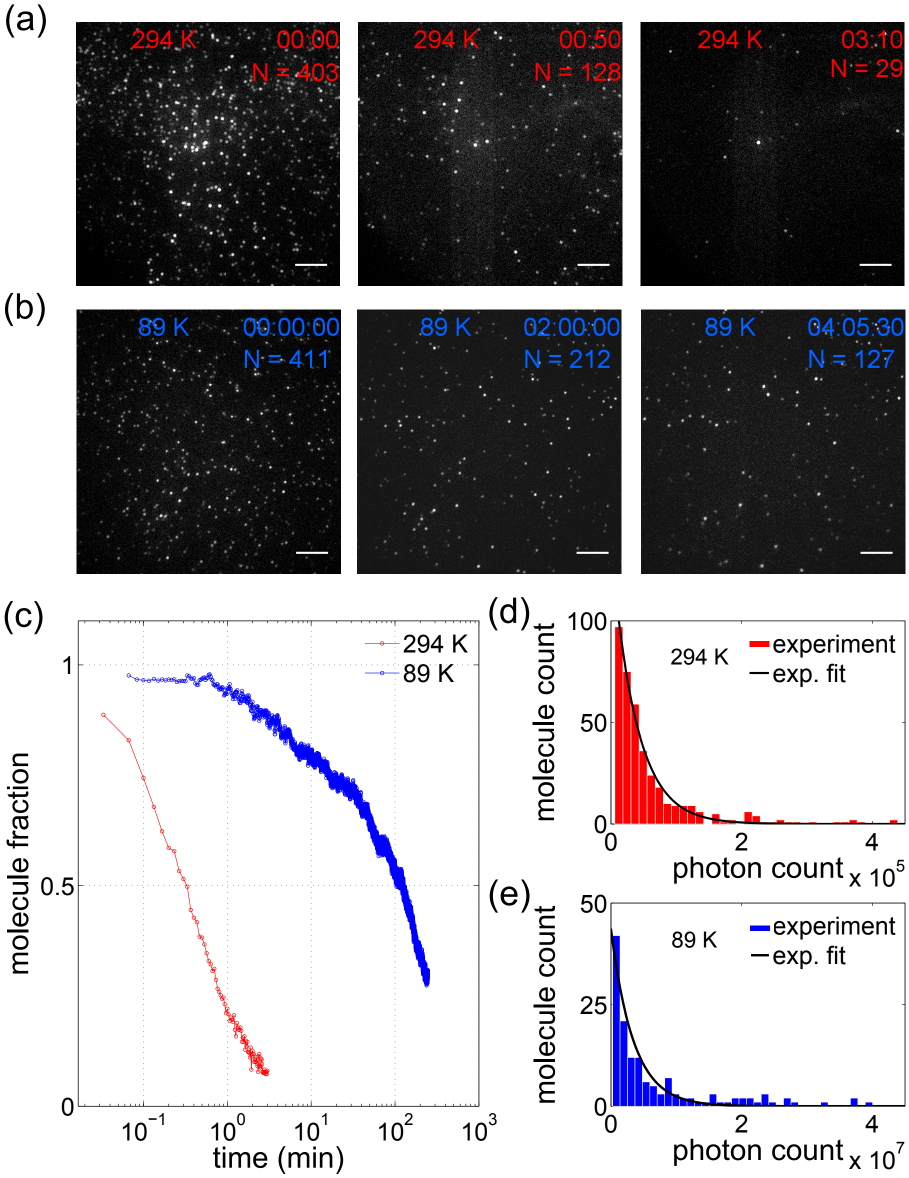

Fig. 7. Photobleaching of Atto647N at 294 K and 89 K. (A, B) The first, middle, and last frame of Media 1 and Media 2. Scale bar 10 µm. (c) Number of molecules in each frame of the movies for both temperatures. (D, E) Total number of detected photons from each molecule until bleaching. The histograms of the photon counts for 294 K and 89 K were fitted to an exponential decay yielding decay constant 2.6×10^{-5} and 2.9×10^{-7}, which convert to an average photon yield of 3.8×10^{4} and 3.5×10^{6}, respectively.

#223365 - $15.00 USD Received 19 Sep 2014; revised 20 Nov 2014; accepted 21 Nov 2014; published 6 Feb 2015

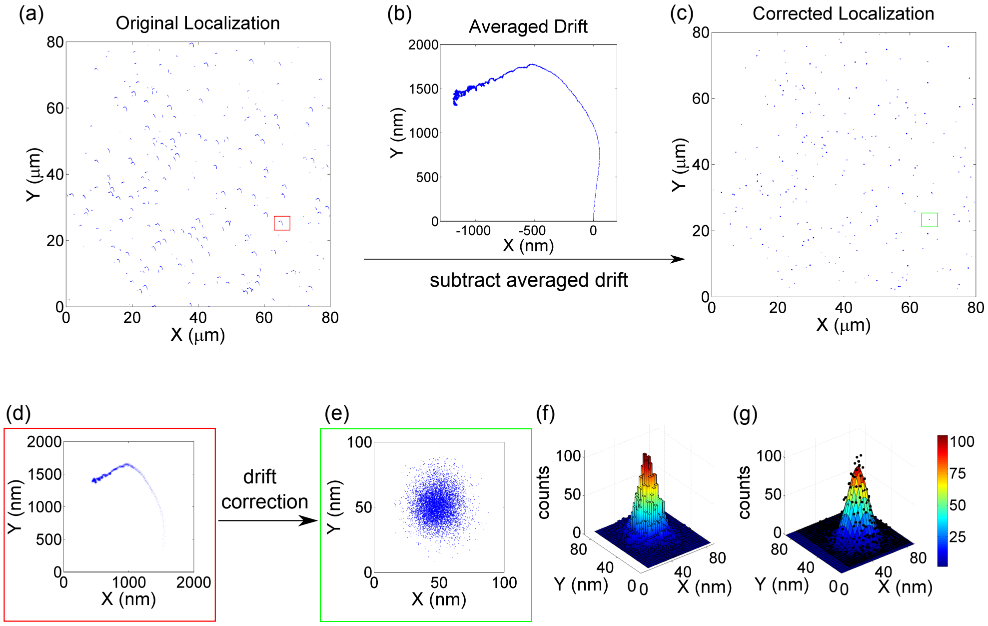

Fig. 8. Drift correction and single molecule localization. (a) Overlay of all localizations of Atto647N molecules imaged at 89 K, as determined with the rapidSTORM software, which displays the sample drift. (b) Averaged position of all localized molecules on each frame, which represents the global sample drift. (c) Drift-corrected localizations. (d) Zoom-in view on the red square in (a), showing a single-molecule trace. (e) Zoom-in view on the green square in (c), showing the drift-eliminated localizations of one molecule. (f) 2D histogram of the localizations in (e). (g) Fit of a 2D Gaussian distribution to the histogram in (f).

factor of ∼380.

Alternatively, we determined the amount of photons detected from each molecule until bleaching (the remaining molecules on the last frame of Media 2 were excluded from this analysis) (Figs. 7(d) and 7(e)). To obtain the number of photons, the PSF of each molecule was fitted to a normalized 2D Gaussian function using the rapidSTORM [26] software. Then, the fitted amplitude A was converted into a photon count number N using a formula provided by the camera manufacturer in the form of $N = (A - b)s/g$, where b is the camera bias, s the device's specific sensitivity, and g the EM-gain. The total number of detected photons until bleaching was computed as the sum of N over all frames for each molecule.

At both temperatures, the histogram of the photon count numbers exhibits an exponential decay, as expected from the theoretical prediction. The average photon yield (obtained from the fitting) increases from 3.8×10^4 at 294 K up to 3.5×10^6 at 89 K, which is an increase by two orders of magnitude. The experiment at 89 K was terminated after four hours when all liquid nitrogen in the cryostat tank had been evaporated (although refill would have been possible), because the collected number of photons was already sufficiently large to localize single molecules with sub-nanometer accuracy (see next section).

4.2. Single Molecule Localization

With the superior photon count numbers per molecule obtained at 89 K, we applied a procedure to localize single fluorescent molecules with sub-nanometer accuracy after drift correction. First, the movie was processed with the freeware rapidSTORM, which returns the positions of

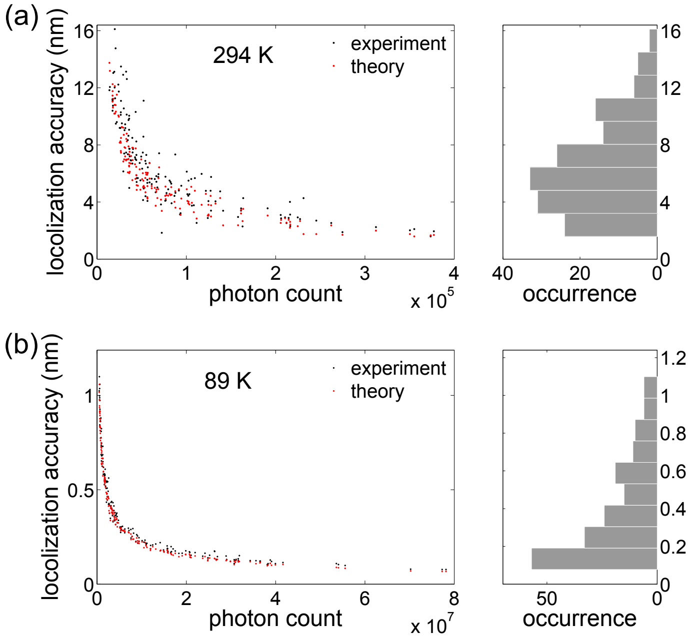

Fig. 9. Comparison of the localization accuracy at 294 K (a) and 89 K (b). The experimentally determined localization accuracy was correlated with photon count numbers, and compared with theoretical predictions [27]. The theoretical values were calculated separately for each molecule to include the influence of the local background, which differs slightly from molecule to molecule.

each localized molecule. The overlay of these localizations displayed the lateral sample drift (Figs. 8(a) and 8(d)). To correct for this drift, the frame-to-frame displacement of all molecules was calculated and averaged for each successive pair of frames, which yielded the average sample drift (Fig. 8(b)). Then, this averaged drift was subtracted from the original positions of the localized molecules. The resulting localizations for each single molecule (Figs. 8(c) and 8(e)) displayed a Gaussian distribution (Figs. 8(f) and 8(g)).

We found that the localization histograms of all molecules could be well fitted with a nearly circular Gaussian distribution with ellipticity values between zero and 10%. This slight ellipticity, with principal axes oriented differently from molecule to molecule, is attributed to a slight residual, position-dependent drift on the order of one nanometer, which is probably due to local heating effects by the exciting laser light. The center position of each fitted Gaussian gives the final localization of the molecule, and the standard deviation (averaged value for the two principal axes of the Gaussian fit) divided by the square root of the number of localizations determines the final localization accuracy.

A comparison of the localization accuracies at 294 K and 89 K is presented in Fig. 9. As the standard error scales inversely proportional with the square root of the number of measurements, the ∼10,000 localizations for more than 80% of the molecules at 89 K converts into a localization accuracy below 1 nm (Fig. 9(b)). In comparison, this value was around 10 nm at 294 K (Fig. 9(a)). Thus, imaging single molecules at 89 K improves the localization accuracy by more than ten times. Furthermore, as represented in Fig. 9, a comparison of the experimentally determined relationship between localization accuracy and number of detected photons with the theoretical predictions derived by Mortensen el al. [27] shows an excellent agreement.

One reason for the superior localization accuracy achieved in our experiments is the excellent mechanical stability of the imaging system, which shows only moderate lateral drift and negligible vertical drift (the sample remained in focus for more than four hours as shown in Fig. 7(b)). The drift correction method that we have applied is very simple and can be always used as long as there are enough single molecule localizations per frame. Alternatively, one can apply a similar procedure by using fiducial fluorescent markers. Our results show that working at a temperature of 89 K is sufficient to enhance the photostability and thus photon count numbers of organic dyes for being able to localize them with an accuracy of better than 1 nm. This opens the possibility of using single molecule localization in wide-field fluorescence microscopy for resolving intramolecular structural details of biomolecules.

5. Conclusion

We have designed and built a versatile, cost-efficient wide-field cryo-fluorescence microscope with exceptionally high thermal and mechanical stability, superior single molecule imaging quality, and the capability of sample change at cryogenic temperatures. We have shown that cooling to liquid nitrogen temperatures is sufficient to boost the photostability of an organic dye such as Atto647N by a factor of $\sim$380 (compared to room temperature). The resulting increase in detectable photons per molecule by more than two orders of magnitude, together with the superior mechanical and thermal stability of the system, allowed for localizing single fluorescent molecules with sub-nanometer accuracy. By using approaches similar to STORM or PALM at cryogenic temperature, we hope that this will enable us to co-localize several molecules with a similar accuracy, which may open the fascinating prospect of using wide-field cryo-fluorescence microscopy for structural biology of single biomolecules or biomolecular complexes.

Acknowledgments

We are grateful to Prof. Dr. Holger Stark, Dr. Martin Wenderoth, Dipl. Ing. Bernhard Spicher, and Dr. Iwan Schaap for their help and the numerous inspiring discussions and constructive suggestions for the design of the cryostat. We thank Dr. Olaf Schulz for his kind assistance with the construction of the optical system. This work was supported by the DFG Cluster of Excellence 'Center for Nanoscale Microscopy and Molecular Physiology of the Brain' (CNMPB), and by a grant of the Deutsche Forschungsgemeinschaft (DFG, SFB 860, project A6).